Supramolecular Heterodimer Peptides Assembly for Nanoparticles Functionalization

Clélia Mathieu, Shayamita Ghosh, Julien Draussin, Adeline Gasser, Guillaume Jacquot, Mainak Banerjee, Tanushree Gupta, Marc Schmutz, Céline Mirjolet, Olivier Tillement, et al.

RESEARCH ARTICLE

ADVANCED HEALTHCARE MATERIALS
www.advhealthmat.de

Supramolecular Heterodimer Peptides Assembly for Nanoparticles Functionalization

*Clélia Mathieu, Shayamita Ghosh, Julien Draussin, Adeline Gasser, Guillaume Jacquot, Mainak Banerjee, Tanushree Gupta, Marc Schmutz, Céline Mirjolet, Olivier Tillement, François Lux, Andrey S. Klymchenko, Mariel Donzeau, Xavier Pivot, Sébastien Harlepp, and Alexandre Detappe**

Nanoparticle (NP) surface functionalization with proteins, including monoclonal antibodies (mAbs), mAb fragments, and various peptides, has emerged as a promising strategy to enhance tumor targeting specificity and immune cell interaction. However, these methods often rely on complex chemistry and suffer from batch-dependent outcomes, primarily due to limited control over the protein orientation and quantity on NP surfaces. To address these challenges, a novel approach based on the supramolecular assembly of two peptides is presented to create a heterotetramer displaying V_HHs on NP surfaces. This approach effectively targets both tumor-associated antigens (TAAs) and immune cell-associated antigens. In vitro experiments showcase its versatility, as various NP types are biofunctionalized, including liposomes, PLGA NPs, and ultrasmall silica-based NPs, and the V_HHs targeting of known TAAs (HER2 for breast cancer, CD38 for multiple myeloma), and an immune cell antigen (NKG2D for natural killer (NK) cells) is evaluated. In in vivo studies using a HER2+ breast cancer mouse model, the approach demonstrates enhanced tumor uptake, retention, and penetration compared to the behavior of nontargeted analogs, affirming its potential for diverse applications.

1. Introduction

The field of nanotechnology has made significant advances in the design and synthesis of functional nanoparticles (NPs) enabling precise control over their assembly and properties.[1,2] Biofunctionalization of these NPs is a well-established technique, facilitating targeted interactions with specific cell types.[3] In oncology, and more specifically in immuno-oncology, this approach is broadly applied to enhance NPs uptake by tumors or to direct them toward specific immune cells.[4–6] However, previously reported studies suggest that the pharmacokinetics and biodistribution of targeted nanoparticles (NPs) are primarily influenced by the inherent physicochemical properties of the NPs themselves rather than the biofunctionalization process.[7,8]

Existing methods of functionalizing NPs with monoclonal antibodies (mAbs) face challenges in achieving controlled NP-to-mAb ratios and site-specific conjugation,

C. Mathieu, S. Ghosh, J. Draussin, A. Gasser, G. Jacquot, M. Banerjee, X. Pivot, S. Harlepp, A. Detappe
Institut de Cancérologie Strasbourg Europe
Strasbourg 67000, France
E-mail: a.detappe@icans.eu

C. Mathieu, S. Ghosh, J. Draussin, A. Gasser, G. Jacquot, M. Banerjee, X. Pivot, S. Harlepp, A. Detappe
Strasbourg Drug Discovery and Development Institute (IMS)
Strasbourg 67000, France

The ORCID identification number(s) for the author(s) of this article can be found under https://doi.org/10.1002/adhm.202304250

DOI: 10.1002/adhm.202304250

C. Mathieu, S. Ghosh, J. Draussin, A. Gasser, G. Jacquot, M. Banerjee, X. Pivot, S. Harlepp, A. Detappe
Equipe labellisée ligue contre le cancer
26 Rue d'Ulm, Paris 75005, France

T. Gupta, A. S. Klymchenko
Laboratoire de Bioimagerie et Pathologies
Université de Strasbourg
UMR 7021 CNRS, Illkirch 67401, France

M. Schmutz
Université de Strasbourg
CNRS
Institut Charles Sadron
UPR 22, Strasbourg 67034, France

C. Mirjolet
Radiation Oncology Department
Preclinical Radiation Therapy and Radiobiology Unit
Centre Georges-François Leclerc
Unicancer, Dijon 21000, France

C. Mirjolet
TIReCS team
INSERM UMR 1231, Dijon 21000, France

which can induce risks associated with heterogeneous batches.[9–12] As an alternative, antibody fragments such as nanobodies derived from llamas, specifically the single variable domain of heavy-chain-only antibodies (V_HHs), offer advantages such as monovalency, hydrophilicity, and specificity toward the targeted antigen.[13] These V_HHs can be directly grafted onto NPs.[14,15] This approach, however, does not allow to prepare rapid-to-screen functionalized NP to target different tumor associated antigens (TAAs) or immune cell antigens and may suffer from batch-to-batch variation from the synthesis of the NP itself.

Another approach to improve batch consistency is to take advantage of the ability of given peptides to self-assemble, such as by using peptide sequences derived from the tetramerization domain of p53.[16] These small peptides, p53tet-K351E (referred to as E3) and p53tet-E343K/E346K (referred to as K3), have the ability to form stable heterotetramers in solution at a 1:1 ratio.[17,18] Building on this knowledge, we engineered various types of V_HHs fused to the *N*-terminal end of the E3 peptide. Taking advantage of click chemistry, we also designed NPs such that the reaction with K3 peptides is favored thermodynamically. Therefore, our E3-K3 functionalization approach enables the generation of a large batch of prefunctionalized NPs@K3 ready to undergo self-assembly with various types of V_HHs through E3-K3 heterotetramerization (**Figure 1A**). This provides precise control over the density of V_HHs on the NPs, while addressing the challenge of synthesizing reproducible batches of NPs with different type of V_HHs at their surface for comparison studies. Furthermore, the presence of abundant K3-E3@V_HH complexes on the NP surface is expected to enhance NP stealth as it has been demonstrated with PEGylated NPs,[19] reducing opsonization and uptake by the reticular endothelial system (RES) compared to that achieved by conventional V_HH-functionalized NPs or by nonfunctionalized NPs.[20]

Though this study, we aimed to validate, both in vitro and in vivo, the self-assembled targeted-NP strategy, thereby creating novel versatile and supramolecular nanoplatforms that target TAAs and immune cell antigens.

2. Results and Discussion

2.1. Synthesis, Characterization, and In Vitro Validation of the Targeting Specificity of the E3@V_HH library

Expanding on E3-K3 heterotetramerization, we have developed a proof-of-concept strategy for generating targeted NPs that are commonly employed in therapeutic and diagnostic applications. Through bio-orthogonal click chemistry,[21] we constructed two libraries: one consisting of NP@K3, including a large panel of NPs, such as ultrasmall lanthanide-based NPs[22] (silica-based bismuth (Si-Bi), silica-based gadolinium (Si-Gd), silica-based holmium (Si-Ho)), and NPs more commonly used in the field of drug delivery, such as liposomes[23] and poly(lactic-*co*-glycolic acid) (PLGA) NPs.[24] These NPs were all functionalized by using dibenzocyclooctyne (DBCO) groups that can react with a K3-azide (K3-N_3) peptide.

In parallel, we also developed E3@V_HHs targeting multiple cell-surface receptors, including ErBb2 (HER2+ breast cancer cells), CD38 (plasma cells), NKG2D ligands (NK cells), and eGFP (control) (Figure 1A; and Figure S1, Supporting Information). E3@V_HH targeting ErbB2 domain 3 (E3@HER2), as well as the other V_HHs, was overexpressed in *E. coli*. with the fusion of a cysteine residue at the *N*-terminal extremity for the further conjugation of a fluorescent dye (FD) by thiol-maleimide chemistry. The purification of these E3@V_HH was based on immobilized metal affinity chromatography (IMAC) followed by size exclusion chromatography (SEC). Furthermore, the purification was validated by sodium dodecyl sulfate–polyacrylamide gel electrophoresis (SDS-PAGE) (Figure 1B; and Figure S2, Supporting Information). The final yields of all the purified recombinant proteins were >0.1 mg mL^{-1}.

To confirm that the functionalization of the V_HHs on the NP surface does not impact the recognition specificity of each V_HH, we tested whether the different parts of the building block process altered the binding affinity of the V_HHs (Figure 1C,D). Hence, the apparent affinity constant (K_D) of each E3-V_HH was determined by flow cytometry using E3@eGFP for normalization. The apparent K_D was 15.1 ± 1.7 nM for E3@HER2 in the HCC-1954 cell line (HER2+ cell line), 22.8 ± 3.6 nM for E3@NKG2D in the NK-92 cell line, and 73.1 ± 2.3 nM for E3@CD38 in the KMS18 cell line (CD38+ myeloma cells) (Figure 1C). These results confirmed that the binding specificity of these V_HHs is not affected by fusion to the E3 peptide.

Then, we conducted thermal shift assays (TSAs) to investigate the self-assembly of the various E3@V_HHs with the K3 peptide. The alterations in melting temperature provided insight into the dynamic interplay between the E3 fusion V_HHs and K3 peptide, ultimately yielding self-assembly dissociation constant (K_D) values. All K_D values were very similar: 12.5 ± 0.1 nM in the case of K3-E3@HER2, 27.3 ± 0.1 nM for K3-E3@NKG2D and 83.8 ± 0.1 μM for K3-E3@CD38 with no statistical differences among the groups (*P*-value>0.05, Mann–Whitney test) (Figure 1D). These results demonstrate that the binding constant of E3-K3 is not altered by the fusion of V_HH to E3.

Finally, we verified whether the apparent K_D previously determined with E3@V_HHs alone remained consistent after heterotetramerization with K3 conjugated to a FD. We first confirmed qualitatively the binding specificity of these FD@K3-E3@V_HHs through confocal imaging (Figure 1E). Next, we determined K_D values of 13.0 ± 1.6, 23.5 ± 2.1, and 75.3 ± 2.4 nM for FD@K3-E3@HER2, FD@K3-E3@NKG2D, and FD@K3-E3@CD38, respectively, using the same cell lines as abovementioned (Figure 1F). The K_D values displayed no statistically significant deviation from their E3@V_HH counterparts (*P*-values > 0.05 for all comparison groups,

O. Tillement, F. Lux
Institut Lumière-Matière
UMR 5306
Université Claude Bernard Lyon1-CNRS
Villeurbanne Cedex France
F. Lux
Institut Universitaire de France (IUF)
Paris 75231, France
M. Donzeau
Institut de génétique et de biologie moléculaire et cellulaire
Illkirch 67404, France

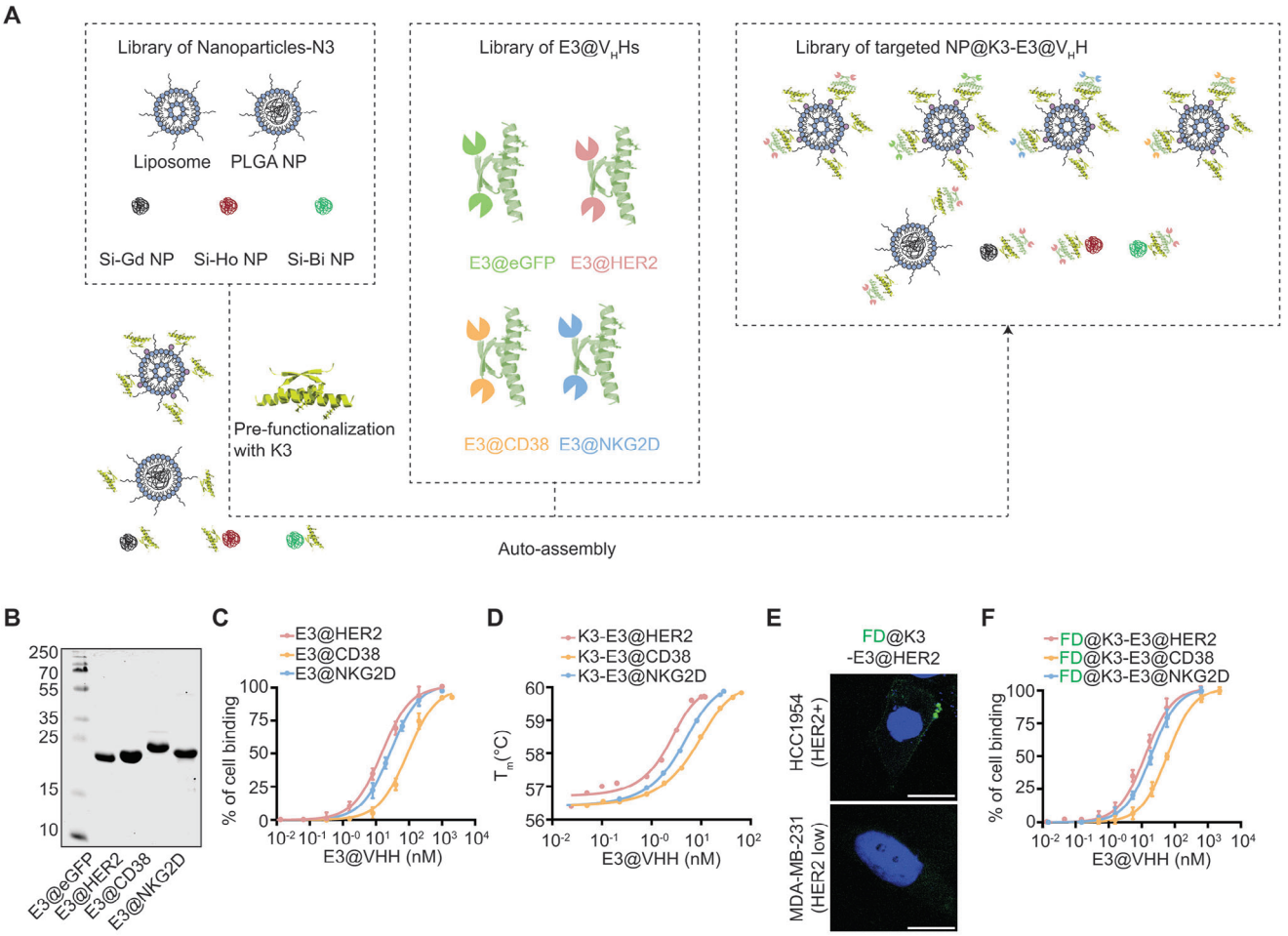

Figure 1. Development of the nanoparticle@K3-E3@V$_H$Hs library. A) Schematic representation of the strategy used to develop the different targeted nanoparticles. B) SDS-PAGE qualitative analysis of purified E3@V$_H$Hs. C) Flow cytometry study determining the apparent binding affinity of the different E3@V$_H$Hs, E3@HER2 on HCC1954, E3@CD38 on KMS18, and E3@NKG2D on NK-92 cell lines. D) Thermal shift assays validating the auto-assembly of the different E3@V$_H$Hs to K3 peptide. E) Fluorescent imaging of the fluorescent dye (FD) Bodipy 493/503@K3-E3@HER2 on HER2+ (HCC1954) and HER2- (MDA-MB-231) cell lines. Nucleus is represented in DAPI (blue) and fluorescent dye (FD) in green. Scale bar = 20 µm. F) Flow cytometry study determining the apparent binding affinity of the different FD@K3-E3@V$_H$Hs; FD@K3-E3@HER2 on HCC1954, FD@K3-E3@CD38 on KMS18, and FD@K3-E3@NKG2D on NK-92 cell lines. Data are presented as mean ± standard deviation and all experiments were performed in triplicates.

Mann–Whitney tests), confirming that coassociation with FD-K3 does not modify the apparent binding efficiency of the V$_H$Hs. Altogether, these results confirmed the suitability of our approach for the prospective development of a targeting strategy.

2.2. Generation of a Self-Assembled Targeted Nanoplatform Library Directed Toward Various Cell Membrane Targets

To assess the adaptability and versatility of this functionalization approach, we embarked on a subsequent investigation aimed at replacing the FD with various types of NPs from our library. In a comprehensive in vitro proof-of-concept analysis, we initially employed liposomes functionalized with HER2 V$_H$Hs. Subsequently, we validated the applicability of these outcomes to other V$_H$Hs and NP types by systematically modulating the experimental conditions (**Figure 2**).

To produce liposome@K3-E3@V$_H$Hs, we initiated the process by conjugating K3-N$_3$ with DSPE-PEG2000-DBCO. The liposomes consisted of a 1:4 ratio of DSPE-PEG2000 and DSPE-PEG2000-DBCO and were formed through a thin-film rehydration method (for further details, see the Experimental Section). Subsequently, the resulting micelles were incubated with K3-N$_3$ at room temperature (RT) overnight, followed by treatment with 0.1% sodium dodecyl sulfate (SDS) to disrupt them. The disassembled micelles were then purified through tangential flow filtration with a cutoff of 5 kDa. The DSPE-PEG2000@K3 conjugate was further introduced into preformulated liposomes (described in the Supporting Information) and allowed to post-insert for 1 h at RT, with a ratio of 2.5 nmol of K3 (DSPE-PEG2000@K3) per milligram of lipids (Figure S3, Supporting Information). Subsequent purification was carried out through tangential flow filtration with a cutoff of 100 kDa to isolate the conjugate liposome@K3-E3@V$_H$Hs, followed by assessment via cryogenic transmission electron microscopy (cryo-TEM)

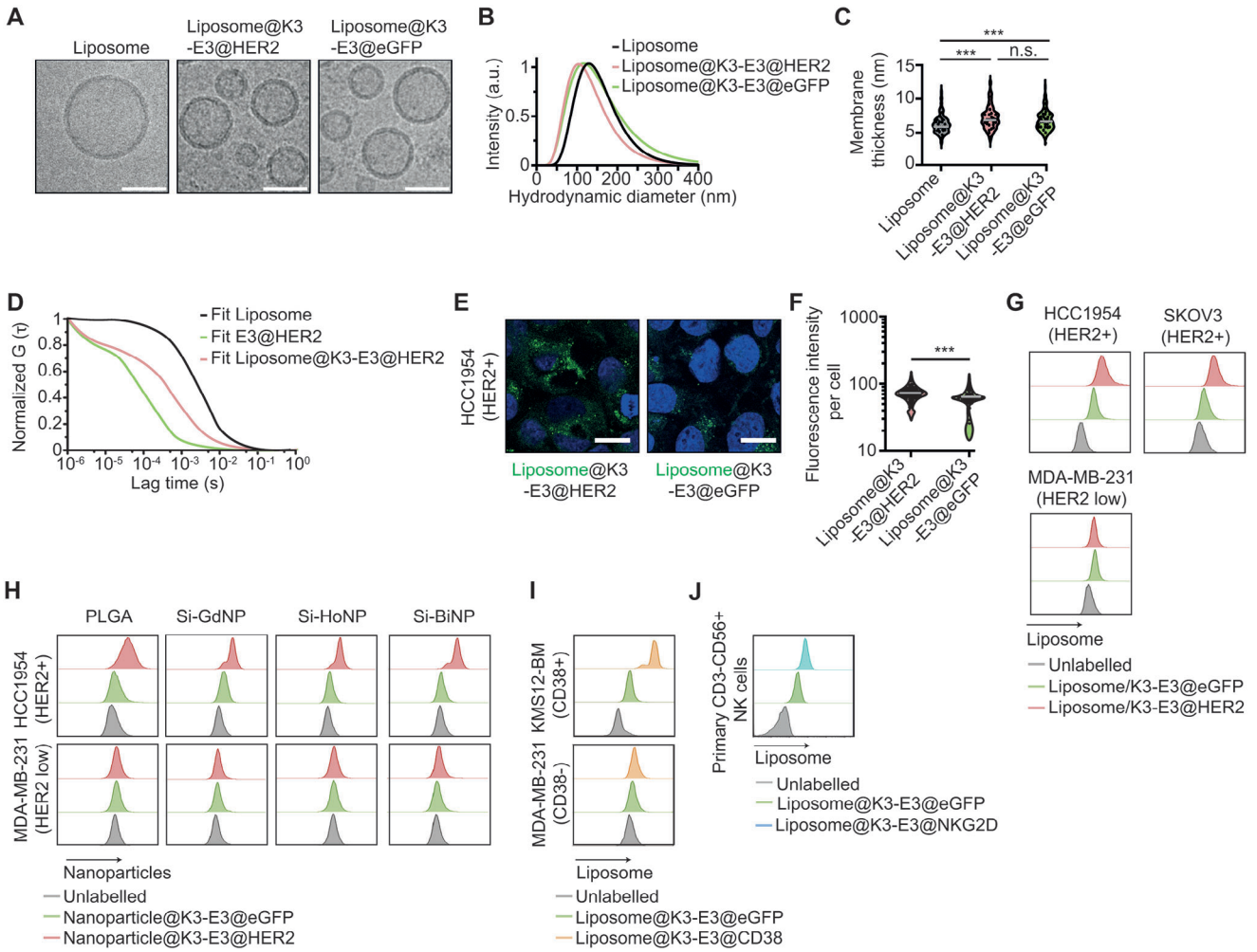

Figure 2. In vitro validation of the different nanoparticles@K3-E3@V_HHs. A) Cryo-TEM images of the liposomes and functionalized liposomes (liposomes@K3-E3@HER2 and liposomes@K3-E3@eGFP). Scale bar = 50 nm. B) Hydrodynamic diameters of the three liposomes measured by dynamic light scattering. C) Membrane thickness quantified based on the cryo-TEM images (n = 150 per group). D) Fluorescent correlation spectroscopy measurements confirming the grafting of E3@V_HHs at the surface of the liposomes. E) Fluorescence imaging of liposome@K3-E3@HER2 and liposome@K3-E3@eGFP on HCC1954 cells. Scale bar = 20 µm. F) Quantification of the fluorescence intensity for both liposomes (n = 100 per group). G) Cell binding specificity determined by flow cytometry of the liposome@K3-E3@HER2 and liposome@K3-E3@eGFP on HER2+ (HCC1954 and SKOV3) as well as on HER2 low (MDA-MB-231) cell lines. H) Cell binding specificity determined by flow cytometry of the various nanoparticles@K3-E3@HER2 and nanoparticles@K3-E3@eGFP on HER2+ (HCC1954) cell line. I) Cell binding specificity determined by flow cytometry of the liposome@K3-E3@CD38 and liposome@K3-E3@eGFP on CD38+ (KMS12-BM) as well as on CD38- (MDA-MB-231) cell lines. J) Cell binding specificity determined by flow cytometry of the liposome@K3-E3@NKG2D and liposome@K3-E3@eGFP on NKG2D+ (primary NK cells) cell line. P-value determined by Mann Whitney tests, *P < 0.05, **P < 0.01, ***P < 0.001. All experiments were performed in triplicates.

(Figure 2A). The size of both the liposomes and liposome@K3-E3@V_HHs was determined through cryo-TEM imaging and the hydrodynamic size was measured by dynamic light scattering (DLS) (Figure 2B). The zeta potential remained consistently stable after functionalization (ζ = −26 and −27 mV before and after functionalization). While the functionalization approach had a negligible impact on the hydrodynamic diameters of the liposomes (DLS size of 112 ± 21 and 121 ± 11 nm; polydispersity index = 0.14 and 0.11, before and after functionalization, respectively), there was a significant increase in the thickness of the liposome membranes before and after the insertion of E3@eGFP or E3@HER2 compared to the membrane thickness of the unmodified liposomes (P value<0.001, Mann–Whitney test), confirming the success of the functionalization strategy (Figure 2C). To characterize the resulting liposome-peptide conjugates, we employed fluorescence correlation spectroscopy (FCS) method, which is commonly used to measure both hydrodynamic diameter and concentration of NPs. Using this approach (Figure 2D; and Figure S4, Supporting Information), we determined an average functionalization of 11 E3@HER2 per liposome.[25,26] Through FCS measurements, the diameter of the liposome was determined to be 87.3 nm, corresponding to the labeled liposomes. The free peptide sample had a diameter of 4.0 nm, which matched its expected hydrodynamic diameter. When the liposome@K3-E3@V_HHs complex was measured, the diameter of the emissive species increased to 31 nm, which

was intermediate between that of the free E3 peptide and the liposome. Moreover, the number of the emissive species nearly doubled compared to that of the liposomes. These data suggested that some fraction of the E3 peptide was grafted to the liposomes, while another fraction remained in the free form. To quantify this result, we performed a fit with two components in which we fixed the correlation times for the free peptide and the liposomes. We found that the component corresponding to the peptide grafted to the liposomes was present at a concentration close to that observed for the liposomes, which confirmed our conclusion that the E3 peptide was successfully grafted onto the liposomes. Nevertheless, the fraction of free peptide was not negligible, although its concentration was much lower than that used in the formulation before the purification of the conjugate. Moreover, one should note that FCS analysis with multiple emissive species of different size provides only semiquantitate result, because it depends on the fitting model and requires fixation of some parameters to obtain reliable and stable fit. Overall, our data provide direct evidence for the conjugation of the E3 peptide to liposomes and the efficiency of the purification method used.

This conjugation methodology was further replicated with various types of NPs, including and ultrasmall lanthanide-based silica NPs (gadolinium, holmium, and bismuth, ≈5 nm[22]) (Figure S5, Supporting Information) and PLGA NPs (≈100 nm) (Figure S6, Supporting Information), to generate a group of ready-to-be functionalized NPs.

After supramolecular assembly at a 1:1 ratio between the amount of K3 and E3-V_HH, the cellular selectivity of the targeted liposomes, specifically toward the TAA ErBb2, was initially assessed through immunofluorescence imaging using HCC-1954 (HER2+) cells. These cells were exposed to liposome@K3-E3@HER2 and liposome@K3-E3@eGFP for 5 min at 4 °C (Figure 2E,F). A statistically significant increase in the fluorescence signal was estimated by confocal imaging in the group treated with liposome@K3-E3@HER2 compared to the group treated with liposome@K3-E3@eGFP (P-value < 0.001, Mann–Whitney test). For a more accurate quantification of the targeting specificity, we next conducted additional experiments using flow cytometry with two HER2+ cell lines (HCC-1954 and SKOV3) and one HER2- cell line (MDA-MB-231) (Figure 2G). The results showed significant binding specificity of the liposome@K3-E3@HER2 for the HER2+ cell lines compared to passive uptake (liposome only) and to control targeted liposomes (liposome@K3-E3@eGFP). No detectable differences were observed between these 3 liposomes in HER2- MDA-MB-231 cells. These results consistently affirmed the heightened specificity of liposome@K3-E3@HER2 toward the TAA ErBb2.

Expanding upon these findings, we next assessed the versatility of this approach by substituting liposomes with other types of NPs while retaining the anti-HER2 V_HH as the targeting unit (Figure 2H). This highlighted the ability of this methodology to efficiently screen a variety of NPs. Finally, we confirmed the comprehensive adaptability of this approach by replacing E3@HER2 with E3@CD38 (Figure 2I) and E3@NKG2D (Figure 2J) on the liposome@K3 platform. In both instances, the functionalized liposomes exhibited specificity toward the targeted antigens, underscoring the potential of these self-assembled targeted nanoplatforms for the rapid screening of different materials and cell target sites.

2.3. In Vivo Confirmation of the Stability of the E3-K3 Heterotetramerization and the Targeting Specificity of the Generated Targeted Nanoplatforms

Although the stability of E3-K3 heterotetramerization has been established in vitro, its suitability for in vivo active targeting remained unproven. We selected liposomes for this in vivo targeting proof-of-concept study due to the extensive published literature on liposomes, which facilitates comparisons with other studies utilizing liposome-full mAbs or liposome fragments of mAbs.[27,28] Given the widespread use of trastuzumab (anti-HER2 mAb) for NP functionalization proof-of-concept studies,[29] we opted to employ E3@HER2 as the targeting component for this in vivo investigation. Consequently, and as previously reported in a meta-analysis comparing passive versus active targeting strategies, our initial goal was to ascertain whether our liposome@K3-E3@HER2 displayed comparable pharmacokinetic and biodistribution properties to nonfunctionalized liposomes in healthy mice and improved tumor targeting efficiency in a HER2+ breast cancer mouse model (**Figure 3A**).

In healthy mice, a single intraperitoneal (ip) administration of either liposomes or liposome@K3-E3@HER2 was conducted to carry out a pharmacokinetic evaluation through the quantification of fluorescence content (Figure 3B). The total amount of liposomes used in this study was confirmed to be nontoxic to the animals at the macroscopic level (Figure S7, Supporting Information). As anticipated, the addition of a targeting unit on the liposome surface did not impact these parameters, resulting in comparable half-lives ($T_{1/2}$, 17.3 ± 2.5 and 22.0 ± 5.1 h, respectively), area under the curve from 0 to 72 h ($AUC_{0\text{-}72\,h}$, 917 ± 273 and 976 ± 110 mg h L^{-1}, respectively), and maximal blood concentration (C_{max}, 49.1 ± 20.1%ID and 43.4 ± 1.0%ID, respectively) (Figure 3C).[7]

Upon performing biodistribution analysis and utilizing ex vivo fluorescence imaging (IVIS, Perkin Elmer) for quantification, we found that over the course of the study, no statistically significant disparities were discerned between passive and active targeted liposomal formulations in the major organs, except for distinctive outcomes in the liver and spleen (26.7 ± 4.7% injected dose per gram of tissue (%ID/g) versus 15.6 ± 3.2%ID/g, P-value for the liver = 0.0095, one-way ANOVA; 16.8 ± 3.2%ID/g versus 7.5 ± 0.4%ID/g, P-value for the spleen = 0.0054, one-way ANOVA) (Figure 3D,E). This variation between targeted and nontargeted liposome formulations can be attributed to a combination of factors. First, it could be explained by the elevated adherence of phospholipids to the liposome surface, making them markedly receptive to uptake by these two specific organs.[30] Furthermore, the presence of an excess of lipoproteins on liposomes can trigger opsonization, a process whereby blood proteins coat the liposomal surface, designating them for swift elimination through the RES, which predominantly comprises the liver and spleen.[31] It is noteworthy that the specific mechanisms may display variations depending on the distinctive attributes of the liposomes and lipoproteins utilized. These points underscore the paramount importance of understanding these interactions for the optimization of drug delivery strategies and the amelioration of potential off-target effects, supporting the need for further investigations.

Next, we sought to validate the targeting specificity of liposome@K3-E3@HER2 and compare it with that of

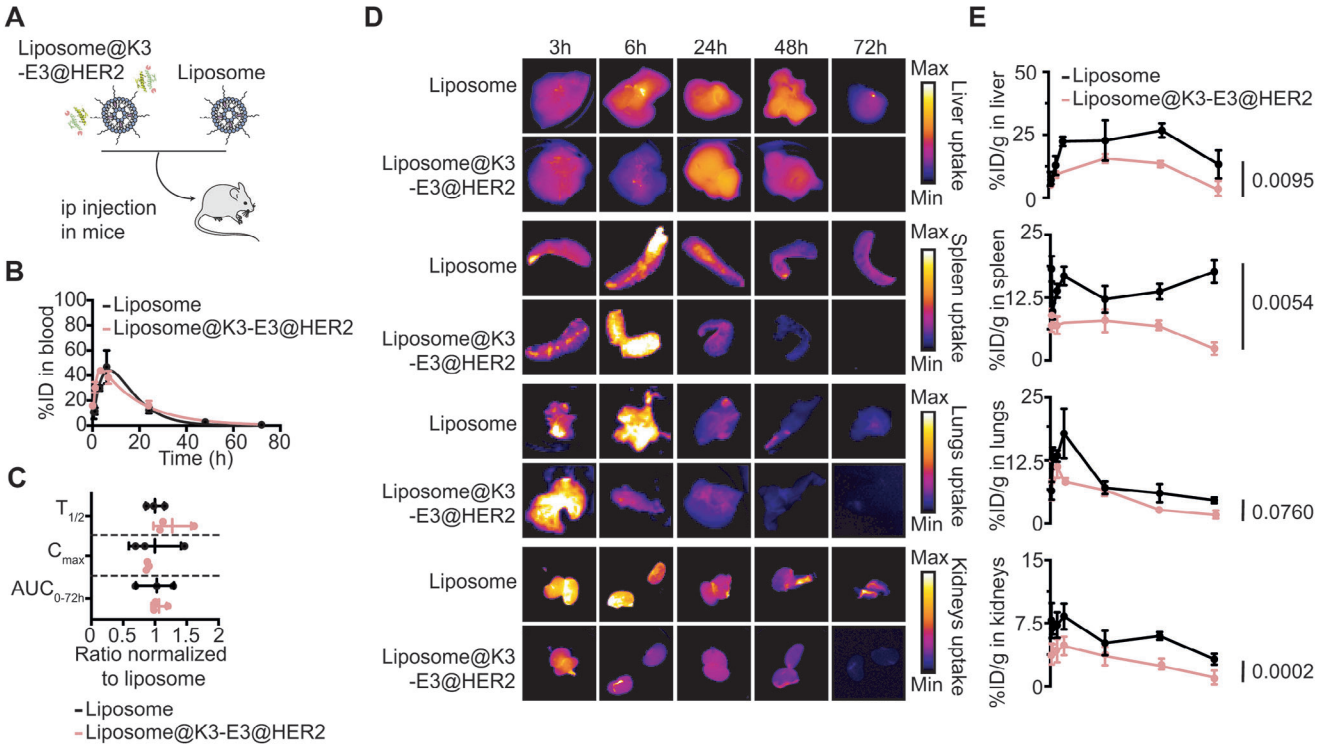

Figure 3. Pharmacokinetic and biodistribution studies of the targeted liposomes. A) Schematic representation of the in vivo study. B) Pharmacokinetic profiles of the liposome and liposome@K3-E3@HER2 intraperitoneally (i.p.) administered in healthy balb/c mice ($n = 6$ per group). C) Comparison of the pharmacokinetic parameters (half-life – $T_{1/2}$; C_{max} – concentration max. in plasma; $AUC_{0\text{-}72\ h}$ – area under the curves between 0 and 72 h post-i.p. administration) normalized to liposome results. D) Fluorescent imaging of the liposomes in major organs 72 h after administration. E) Longitudinal quantification of the nanoparticles' concentration in the major organs ($n = 6$ per group). Data are presented as mean ± standard deviation. *P*-value determined by one-way ANOVA. All experiments were performed on $N = 3$ mice per group.

liposome@K3-E3@eGFP and nonfunctionalized liposomes using a HER2+ subcutaneous xenograft tumor model. We conducted a tumor uptake study by monitoring longitudinally the fluorescence levels present in the tumor by using an IVIS imaging platform (**Figure** 4A,B). The results from this study showed that the maximum tumor uptake was not significantly different from that of liposome@K3-E3@HER2 and liposome or liposome@K3-E3@eGFP (4.01 ± 1.2%ID, 3.4 ± 0.9%ID, and 2.7 ± 1.1%ID, respectively, *P*-value = 0.1143 and 0.057, respectively, Mann–Whitney). However, similar to previously reported results,[6,7] the utilization of active targeting represents a pivotal advancement in achieving substantial tumor retention for an extended period of time, thereby reaffirming the efficacy of this active targeting strategy with significant differences between targeted and nontargeted liposomes from 24 h after i.p. administration (liposome@K3-E3@HER2 versus liposome, *P*-value = 0.028, Mann–Whitney) (Figure 4B). This difference was maintained at 48 h after administration (*P*-value = 0.028, Mann–Whitney). Hence, the employment of an active targeting moiety notably enriched tumor retention, which we predominantly attributed to enhanced tumor penetration. Furthermore, through the use of a colorimetric map delineating NP uptake, we observed that liposome@K3-E3@HER2 displayed considerably deeper tumor penetration than unconjugated liposomes which remained predominantly confined to the tumor periphery, coinciding with regions of heightened neovascularization while the targeted liposome seemed to almost homogeneously distribute within the tumor (Figure 4C,D; and Figure S8, Supporting Information), offering large potential for further drug delivery applications.

3. Conclusion

In conclusion, our research establishes the practical viability of using peptide building blocks for NP functionalization. Tumor uptake closely aligns with conventional mAb-NP strategies, reinforcing the promise of our approach while addressing the usual challenges associated to this common functionalization strategies; mAb-NPs provide precise target recognition, but challenges such as controlling mAb orientation and maintaining the optimal NP-to-mAb ratio impede progress. Additionally, larger mAb-NP complexes hinder effective tumor penetration compared to fragment-NPs.

In our study, we introduced a novel peptide-based strategy for NP functionalization and V_HH screening, demonstrating exceptional tissue penetration due to smaller antibody fragments. This approach offers advantages, such as ease of synthesis and cost-effectiveness, particularly with nonhuman-derived antibody fragments. Our peptide-based building block strategy proves stable in preclinical mouse models. The strong affinity between E3 and K3 peptides suggests applications in a broad range of therapeutic applications which may include drug delivery,

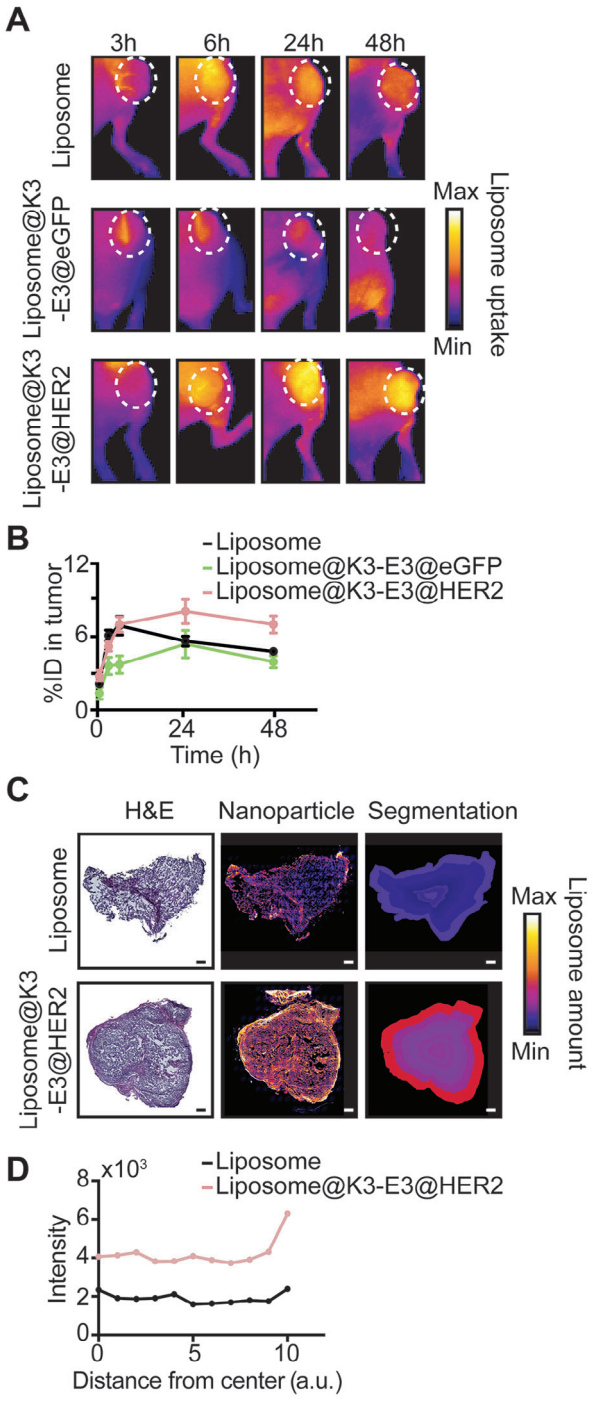

Figure 4. Improved tumor retention of targeted liposomes. A) Longitudinal tumor uptake fluorescence imaging of liposome, liposome@K3-E3@eGFP, and liposome@K3-E3@HER2 groups (n = 5 per group) in HER2+ (HCC1954 cells) subcutaneous breast cancer tumors. B) Longitudinal tumor uptake quantification. C) Hematoxylin and eosin (H&E) staining, nanoparticles uptake (fluorescence signal), and segmentation map of the nanoparticle penetration in the tumor. Scale bar = 200 µm. D) Quantification of the liposome and liposome@K3-E3@HER penetration profile in the tumor. Data are presented as mean ± standard deviation. n.s. denotes nonsignificant; *, P-value < 0.05, **, P-value < 0.01, ***, P-value < 0.001, Mann–Whitney tests. Studies were performed with N = 6 mice per group.

imaging, and immunooncology. In essence, our exploration of peptide building blocks for NP functionalization delivers promising results, highlighting them as a compelling alternative to traditional fragment-NP and mAb-NP methods.

4. Experimental Section

Synthesis of the Nanoparticles: All synthesis details are provided in the Supporting Information. The peptide p53tet-E343K/E346K-azido-PEG4-Nter was purchased through Polypeptide Group, France using the sequence: Asn-Asn-Thr-Ser-Ser-Ser-Pro-GIn-Pro-Lys-Lys-Lys-Pro-Leu-Asp-Gly-Glu-Tyr-Phe-Thr-Leu-GIn-Ile-Arg-Gly-Arg-Glu-Arg-Phe-Glu-Met-Phe-Arg-Lys-Leu-Asn-Lys-Ala-Leu-Glu-Leu-Lys-Asp-Ala-GIn-Ala-Gly-Lys-Glu-Pro-Gly conjugated with Azido-PEG4-C2-carboxylic acid at the *N*-terminus, TFA salt with a purity set at ≥90% and validated by RP-HPLC.

Dynamic Light Scattering (DLS): DLS measurements were conducted using a nano-ZS instrument (Malvern). The suspensions of NPs were prepared in a solution of nanopure water (Milli-Q) at a concentration of 1 mg mL^{-1}. DLS measurements were performed in sets of 10 acquisitions. The average hydrodynamic diameters of the NPs were determined by analyzing the DLS correlation function through a regularization fitting method.

Cryogenic Transmission Electron Microscopy (Cryo-TEM): Liposomal formulations were imaged by cryo-TEM using a previously reported method. Briefly, sample solutions were prepared at 5 mg mL^{-1} in water. A volume of 5 µL was applied to 400 mesh copper TEM grids covered with a lacey carbon film for solutions containing up to 23% water. The grids were freshly glow discharged to make them hydrophilic (Elmo, Cordouan Technologies, Pessac, France). Then, the grids were blotted and immersed into liquid ethane using a homemade freezing machine equipped with a controlled temperature and humidity chamber (set at 22 °C and > 80% relative humidity). For a water content below 23%, no humidity regulation was applied. The grids were then mounted onto a Gatan 626 cryoholder and observed under reduced dose conditions using a Tecnai G2 microscope (FEI) operating at 200 kV. The images were recorded with a slow-scan CCD camera (Eagle 2k2k, FEI).

Fluorescence Correlation Spectroscopy (FCS): To determine the amount of E3@V_HHs per NP, an FCS study was performed. Measurements were performed on a home-built confocal setup based on a Nikon inverted microscope with a Nikon 60 × 1.2 NA water immersion objective.[32] Excitation was provided by a continuous wave laser diode (488 and 638 nm, Oxxius), and photons were detected with a fibered avalanche photodiode (APD SPCM-AQR-14-FC, PerkinElmer) connected to an online hardware correlator (ALV7000-USB, ALV GmbH, Germany). The solution of liposomes was diluted 20 times and peptides were diluted 100x before depositing 200 µL on 96-well optical-bottom plates for measurements. The data were analyzed using PyCorrFit software.

In Vitro Experiments: Cell lines. Human breast cancer cells (MDA-MB-231, HCC-1954) were obtained from American Type Culture Collection (ATCC, USA). Myeloma cancer cells (MM.1S, KMS12-BM, KMS18), and ovarian cancer cells (SKOV3) were generously provided by the Ghobrial Laboratory (Dana-Farber Cancer Institute, Boston, MA). Fetal bovine serum (FBS) was purchased from VWR. MDA-MB-231, KMS18, KMS12-BM, and MM.1S cell lines were cultured in RPMI 1640 with *L*-glutamine (#L0500-500, VWR, France). HCC-1954 and SKOV3 cells were cultured in RPMI 1640 with *L*-glutamine and HEPES (#10-041-CV/702523, Dutsher). All media were supplemented with 10% FBE and 10 000 unit mL^{-1} penicillin and streptomycin (PS, #P06-07100, Dutsher). All cell lines were maintained in a humidified incubator supplied with 5% CO_2, maintained at 37 °C and regularly tested for mycoplasma contamination.

In Vitro Binding Specificity: The in vitro specificity of the different NP@K3-E3@V_HH formulations was assessed using flow cytometry and fluorescence microscopy. For flow cytometry analysis, 1–2.10^5 cells per condition were treated with 100 µL of NPs (ranging from 100 nM to 1 µM) in FACS buffer (PBS, FBS 2%, EDTA 2 mM) for 5 min at room temperature (RT). The cells were then washed three times with PBS, with centrifugation at 300 × g for 5 min between each wash. Flow cytometry data acquisition

was performed using the MACSQuant Analyzer 10 Flow Cytometer (Miltenyi), and subsequent analysis was carried out using FlowJo software (V. 10.8.2).

Fluorescence microscopy was conducted to confirm the localization of NP binding to the cells. A total of 10^5 cells per well were seeded on coverslips in a 12-well plate and incubated overnight. After incubation, the cells were washed twice with PBS and fixed with 4% PFA for 20 min at RT, followed by two additional washes with PBS. The coverslips were mounted using DAPI-containing antifade mounting media (# P36971, Prolong, ThermoFisher, France). DAPI and Bodipy 493/503 (Thermo Fisher) showed blue and green staining, respectively. The images were acquired on an Olympus confocal spinning disk microscope. The 405 and 488 nm wavelengths were evaluated to excite the two probes and an Orca Flash IV camera to record the images. The fluorescence imaging was then analyzed using Fiji software (V. 2.14.0).

In Vivo Experiments: All animal procedures were conducted in compliance with the Guidelines for the Care and Use of Laboratory Animals, as outlined by the Institutional Care and Use Committee (D67-2018-38 and E67-482-041) of the University of Strasbourg (APAFIS: # 38306-2022082410083076 V5). Adult female BALB/c and BALB/c nude mice (Charles River, France; 6–8 weeks old) were acclimated upon arrival, maintained at a constant temperature of 22 °C, and exposed to a 12–12 h light-dark cycle for a minimum of 7 days before any experimentation was initiated. They were kept in a pathogen-free environment with continuous access to food and water throughout the experimental procedures.

Pharmacokinetic and Biodistribution Studies in Healthy Mice: Pharmacokinetic and biodistribution studies were conducted in healthy mice following ip injections of 0.03 µmole kg^{-1} (based on dye amount) liposomes and Liposome@K3-E3@HER2. The mice were euthanized at various time points: 30 min, 1, 3, 6, 24, 48, and 72 h, with three mice per group at each time point. Blood samples were collected via cardiac puncture after euthanasia and stored in EDTA-coated tubes. Simultaneously, all harvested organs were imaged ex vivo using an IVIS system (PerkinElmer). The blood samples were subjected to fluorescence imaging using IVIS to analyze blood-compartment pharmacokinetics (PK), which were then fitted into a two-component model using standard procedures. The protein contents of tissue homogenate samples were determined using the BCA Protein Assay Kit (Thermo Fisher Scientific). To quantify tissue fluorescence and generate biodistribution profiles, the collected organ homogenates were transferred to a 96-well plate and subjected to fluorescence imaging following the same experimental procedure.

Tumor Uptake Study: A total of $1{,}5.10^6$ HCC-1954-Luc+ cells were mixed at a 1:1 ratio v/v with growth factor-reduced Matrigel (Perkin Elmer) and injected subcutaneously into the flanks of the mice to generate tumors. Tumor volume was measured using calipers and calculated as $[(\text{width})^2 \times \text{length}]/2$. Mice were randomly assigned to study groups once the tumor reached 150 mm^3 in volume. Mice were then i.p. administered liposomes, liposome@K3-E3@eGFP or liposome@K3-E3@HER2 at an amount of 3.8 µmoles. Using the same timepoints as for the PK and biodistribution study, tumors were harvested ($n = 3$/time point) and imaged by IVIS. Quantification was performed using the previously described approach.

Ex Vivo Distribution Analysis of the NPs in the Tumor: Tumors previously fixed in 4% paraformaldehyde were sliced into 8 µm sections before being imaged using an in-house designed confocal spinning disk microscope. The V_HHs were excited with a 740 nm laser, and the images were captured using a Hamamatsu Orca Flash camera. Subsequently, the images were stitched together and analyzed using Fiji software (v2.14). The initial region of interest (ROI) was defined based on the contour of the tumor intensity. Then an 8-step sequential scaling factor of 0.8x was applied to reduce the ROI size to the center of the tumor. The average intensity per pixel within these intervals was subsequently analyzed and plotted.

Statistical Analysis: Data are represented as mean ± standard deviation. All results were analyzed using GraphPad Prism 9.5.1. Statistical analysis was performed using unpaired nonparametric *t*-test for multiple groups comparison at a specific time point (Mann–Whitney test) or a one-way ANOVA for group comparison. Significance was determined at the following cutoff points: $^*P < 0.05$, $^{**}P < 0.01$, and $^{***}P < 0.001$.

Supporting Information

Supporting Information is available from the Wiley Online Library or from the author.

Acknowledgements

This research was funded, in part, by the European Research Council (ERC) Starting Grant TheranoImmuno, Grant Agreement No. 95010 (A.D.), the Institut de Cancérologie Strasbourg Europe (A.D., C.M.), ITMO cancer of Aviesan within the framework of the 2021–2030 Cancer Control Strategy, on funds administered by Inserm (A.D.), and the Fondation Française pour la Recherche contre le Myélome et les Gammapathies (FFRMG) (A.D.), and the Ligue contre le cancer (A.D.). The authors also acknowledged the Strasbourg Drug Discovery and Development Institute (IMS) for funding this study, as part of the Interdisciplinary Thematic Institute (ITI) 2021–2028 program of the University of Strasbourg, CNRS and Inserm, IdEx Unistra (ANR-10-IDEX-0002), and by the SFRI-STRAT'US project (ANR-20-SFRI-0012) under the framework of the French Investments for the Future Program (A.D., S.H.). Additionally, the authors acknowledged support from Pascal Kessler at the PIC-STRA imaging platform from the University of Strasbourg. Authors acknowledged the work from E Moeglin who designed the original VHHs used in this manuscript.

Conflict of Interest

The authors declare no conflict of interest.

Author Contributions

C.M. and S.G. contributed equally to this work. C.M., S.G., J.D., A.G., M.B., E.M., C.M., T.G., A.K., M.S., and S.H. performed the experiments. C.M., A.K., X.P., S.H., and A.D. designed the study and analyzed the results. A.D., X.P., M.D., and S.H. wrote the manuscript.

Data Availability Statement

The data that support the findings of this study are available from the corresponding author upon reasonable request.

Keywords

auto-assembly, biofunctionalization, nanomedicine, peptide

Received: December 1, 2023
Revised: January 22, 2024
Published online: March 10, 2024

[1] M. J. Mitchell, M. M. Billingsley, R. M. Haley, M. E. Wechsler, N. A. Peppas, R. Langer, *Nat. Rev. Drug Discovery* **2020**, *20*, 101.
[2] R. Mout, D. F. Moyano, S. Rana, V. M. Rotello, *Chem. Soc. Rev.* **2012**, *41*, 2539.
[3] H. S. Choi, W. Liu, F. Liu, K. Nasr, P. Misra, M. G. Bawendi, J. V. Frangioni, *Nat. Nanotechnol.* **2010**, *5*, 42.
[4] V. Mittelheisser, M. Banerjee, X. Pivot, L. J. Charbonnière, J. Goetz, A. Detappe, *Adv. Therap.* **2020**, *3*, 2000134.
[5] A. M. Sofias, F. Combes, S. Koschmieder, G. Storm, T. Lammers, *Drug Discovery Today* **2021**, *26*, 1482.

[6] L. S. L. Price, S. T. Stern, A. M. Deal, A. V. Kabanov, W. C. Zamboni, *Sci. Adv.* **2020**, *6*, eaay9249.
[7] V. Mittelheisser, P. Coliat, E. Moeglin, L. Goepp, J. G. Goetz, L. J. Charbonnière, X. Pivot, A. Detappe, *Adv. Mater.* **2022**, *34*, 2110305.
[8] L. B. Carmès, M. P. Coliat, S. Harlepp, X. Pivot, O. Tillement, F. Lux, A. Detappe, *Adv. Therap.* **2023**, *6*, 2370024.
[9] M. Bruckner, J. Simon, K. Landfester, V. Mailander, *Nanoscale* **2021**, *13*, 9816.
[10] D. C. Julien, S. Behnke, G. Wang, G. K. Murdoch, R. A. Hill, *mAbs* **2011**, *3*, 467.
[11] A. Detappe, M. Reidy, Y. Yu, C. Mathieu, H. V.-T. Nguyen, T. P. Coroller, F. Lam, P. Jarolim, P. Harvey, A. Protti, Q.-D.e Nguyen, J. A. Johnson, Y. Cremillieux, O. Tillement, I. M. Ghobrial, P. P. Ghoroghchian, *Nanoscale* **2019**, *11*, 20485.
[12] E. Thomas, C. Mathieu, P. Moreno-Gaona, V. Mittelheisser, F. Lux, O. Tillement, X. Pivot, P. P. Ghoroghchian, A. Detappe, *Adv. Healthcare Mater.* **2022**, *11*, e2101565.
[13] A. C. Marques, P. J. Costa, S. Velho, M. H. Amaral, *J. Controlled Release* **2020**, *320*, 180.
[14] D. Schmid, C. G. Park, C. A. Hartl, N. Subedi, A. N. Cartwright, R. B. Puerto, Y. Zheng, J. Maiarana, G. J. Freeman, K. W. Wucherpfennig, D. J. Irvine, M. S. Goldberg, *Nat. Commun.* **2017**, *8*, 1747.
[15] Y.u-S. S. Yang, K. D. Moynihan, A. Bekdemir, T. M. Dichwalkar, M. M. Noh, N. Watson, M. Melo, J. Ingram, H. Suh, H. Ploegh, F. R. Stellacci, D. J. Irvine, *Biomater. Sci.* **2018**, *7*, 113.
[16] R. D. Brokx, E. Bolewska-Pedyczak, J. Gariepy, *J. Biol. Chem.* **2003**, *278*, 2327.
[17] M. Vigneron, F. Dietsch, L. Bianchetti, A. Dejaegere, Y. Nominé, A. Cordonnier, G. Zuber, B. Chatton, M. Donzeau, *Bioconjug. Chem.* **2019**, *30*, 1734.
[18] A. Stoessel, N. Groysbeck, L. Guyot, L. Barret, Y. Nominé, L. Nguekeu-Zebaze, A. Bender, L. Voilquin, T. Lutz, N. Pallaoro, M. Blocat, C. Deville, M. Masson, G. Zuber, B. Chatton, M. Donzeau, *Bioconjug. Chem.* **2020**, *31*, 2421.
[19] S. D. Li, L. Huang, *J. Controlled Release* **2010**, *145*, 178.
[20] C. D. Walkey, J. B. Olsen, H. Guo, A. Emili, W. C. Chan, *J. Am. Chem. Soc.* **2012**, *134*, 2139.
[21] E. M. Sletten, C. R. Bertozzi, *Angew. Chem., Int. Ed. Eng.* **2009**, *48*, 6974.
[22] V.u-L. Tran, V. Thakare, F. Rossetti, A. Baudouin, G. Ramniceanu, B.-T. Doan, N. Mignet, C. Comby-Zerbino, R. Antoine, P. Dugourd, F. Boschetti, F. Denat, C. Louis, S. Roux, T. Doussineau, O. Tillement, F. Lux, *J. Mater. Chem. B* **2018**, *6*, 4821.
[23] F. Sauvage, S. Franzè, A. Bruneau, M. Alami, S. Denis, V. Nicolas, S. Lesieur, F.-X. Legrand, G. Barratt, S. Messaoudi, J. Vergnaud-Gauduchon, *Int. J. Pharm.* **2016**, *499*, 101.
[24] L. Zhang, J. M. Chan, F. X. Gu, J.-W. Rhee, A. Z. Wang, A. F. Radovic-Moreno, F. Alexis, R. Langer, O. C. Farokhzad, *ACS Nano* **2008**, *2*, 1696.
[25] K. Koynov, H.-J. Butt, *Curr. Opin. Colloid Interface Sci.* **2012**, *17*, 377.
[26] A. S. Klymchenko, E. Roger, N. Anton, H. Anton, I. Shulov, J. Vermot, Y. Mely, T. F. Vandamme, *RSC Adv.* **2012**, *2*, 11876.
[27] M. Riaz, M. Riaz, X. Zhang, C. Lin, K.a Wong, X. Chen, G.e Zhang, A. Lu, Z. Yang, *Int. J. Mol. Sci.* **2018**, *19*, 195.
[28] G. T. Noble, J. F. Stefanick, J. D. Ashley, T. Kiziltepe, B. Bilgicer, *Trends Biotechnol.* **2014**, *32*, 32.
[29] I. Steinhauser, B. Spankuch, K. Strebhardt, K. Langer, *Biomaterials* **2006**, *27*, 4975.
[30] N. Bertrand, P. Grenier, M. Mahmoudi, E. M. Lima, E. A. Appel, F. Dormont, J.-M. Lim, R. Karnik, R. Langer, O. C. Farokhzad, *Nat. Commun.* **2017**, *8*, 777.
[31] V. P. Torchilin, V. G. Omelyanenko, M. I. Papisov, A. A. Bogdanov, V. S. Trubetskoy, J. N. Herron, C. A. Gentry, *Biochim. Biophys. Acta* **1994**, *1195*, 11.
[32] A. Reisch, D. Heimburger, P. Ernst, A. Runser, P. Didier, D. Dujardin, A. S. Klymchenko, *Adv. Funct. Mater.* **2018**, *28*, 1805 157.